50th AIAA Aerospace Sciences Meeting including the New Horizons Forum and Aerospace Exposition
09 - 12 January 2012, Nashville, Tennessee

AIAA 2012-0532

Modeling Ablation of Charring Heat Shield Materials For Non-Continuum Hypersonic Flow

Erin D. Farbar* and Iain D. Boyd †

Department of Aerospace Engineering, University of Michigan, Ann Arbor, MI 48109

Alexandre Martin ‡

Department of Mechanical Engineering, University of Kentucky, Lexington, KY 40506

We describe the on-going development of physical models for use with the direct simulation Monte Carlo (DSMC) method that allow the injection of pyrolysis gases generated by the ablation of charring thermal protection system material for flows in translational nonequilibrium. The test case used in the study is the Stardust reentry capsule, which employed a Phenolic Impregnated Carbon Ablator (PICA) heat shield and experienced very high heat loads during its descent through the atmosphere of the Earth. We systematically examine the effect of improving the level of sophistication of the physical models used for chemical reactions, surface temperature, and ablative mass flux on the predicted flowfield and surface properties.

I. Introduction

Many of the future thermal protection materials of interest to NASA for atmospheric reentry are ablators. When a charring ablator is used, thermal pyrolysis of the heat shield material produces a gas which flows through the surface and into the flowfield, and the exposed surface of the material reacts and eventually loses mass and recesses. At high altitude, the majority of the ablative products come from the inner structure of the material.[1] The pyrolysis process starts early in the reentry trajectory, often when the vehicle has not yet reached the continuum regime. The direct simulation Monte Carlo (DSMC) method can be used in this non-continuum regime to simulate the interaction of the flowfield with the ablation products.

Modeling hypersonic flowfields including ablation is an active area of research and the body of literature in this area is increasing accordingly. In this study, we focus specifically on work involving the charring ablative material, Phenolic Impregnated Carbon Ablator (PICA), used on the Stardust sample return capsule and on the Mars Science Laboratory mission. Olynick et al.[2] and Martin and Boyd[3] produced axisymmetric solutions of the Stardust reentry flowfield at various points along the reentry trajectory using Computational Fluid Dynamics (CFD) codes coupled to material response codes. Zhong et al.[4] obtained axisymmetric DSMC solutions of the Stardust flowfield at the 81 km flight condition, utilizing a set of chemical reaction rates that were developed for simulation of Mars entries. They estimated the composition of the pyrolysis gas using the predicted mass fractions of species at the stagnation point obtained from a previous CFD calculation,[2] and included surface reactions in their simulations. In these cases, an assumption of chemical equilibrium between the boundary layer gases, the pyrolysis gas being emitted from the vehicle surface, and the surface itself was used to determine the composition of the gas at the surface of the vehicle.

We are currently focused on implementing physical models required to simulate an ablative boundary condition for nonequilibrium hypersonic flows using the DSMC method. We are starting the process by first simulating the ejection of the pyrolysis gas produced during the ablation process into the flowfield. This also involves implementing the capability to simulate carbon and hydrogen species and the associated chemical reactions, as well as polyatomic species, with the DSMC method. The Stardust 81 km flight condition is chosen as the initial test case because that vehicle utilized a charring ablator, and because

*Research Fellow, Member AIAA. Email: efarbar@umich.edu
†James E. Knott Professor of Engineering, Fellow AIAA. Email: iainboyd@umich.edu
‡Professor, Member AIAA.

radiation spectra were obtained during reentry that can be used for partial validation of the results. This paper details the implementation of the blowing boundary condition, variable surface temperature and mass flux boundaries, and the chemical reaction mechanism including hydrogen and carbon species in a state-of-the-art DSMC code developed at the University of Michigan. Full-body, axisymmetric flowfield results are compared for the following cases: with and without ablation effects included, with constant and variable wall temperature profiles and blowing rates, with and without recombination reactions modeled, and with and without ionization effects included. The paper ends with some conclusions and suggestions for future work.

II. Details of the baseline DSMC model

The numerical simulations are performed using the DSMC code MONACO,[5] currently being developed at the University of Michigan. The Variable Hard Sphere (VHS) model is used to simulate particle interactions.[6] Models for rotational[7] and vibrational[8] relaxation during inelastic collisions are included. The reaction rate coefficients used to model chemical reactions between air species using the Total Collision Energy (TCE) chemistry model are compiled using References 9, 10, 11 and 12 and listed in Tables 1 and 2. Additionally, the Vibrationally Favored Dissociation (VFD) chemistry model[13] is used to model the preferential dissociation of N_2 and O_2 molecules from higher vibrational states using preferential parameter values of 2.0 and 0.5, respectively.

Table 1: Reaction rate coefficients (m^3/molecule/s) used in the TCE chemistry model for reactions involving neutral species.

Number	Reaction	Rate Coefficient
1Mf[a]	N_2+M→N+N+M	$1.162\times10^{-8}T^{-1.6}\exp(-113\ 200/T)$
1Mb	N + N + M → N_2 + M	$1.072\times10^{-39}T^{-1.6}$
1Af[b]	N_2+A→N+N+A	$4.980\times10^{-8}T^{-1.6}\exp(-113\ 200/T)$
1Ab	N + N + A → N_2 + A	$4.597\times10^{-39}T^{-1.6}$
1E[c]	N_2+e^-→N+N+e^-	$4.980\times10^{-6}T^{-1.6}\exp(-113\ 200/T)$
2Mf	O_2+M→O+O+M	$3.321\times10^{-9}T^{-1.5}\exp(-59\ 400/T)$
2Mb	O + O + M → O_2 + M	$4.597\times10^{-42}T^{-1.0}$
2Af	O_2+A →O+O+A	$1.660\times10^{-8}T^{-1.5}\exp(-59\ 400/T)$
2Ab	O + O + A → O_2 + A	$2.298\times10^{-41}T^{-1.0}$
3Mf	NO+M→N+O+M	$8.302\times10^{-15}\exp(-75\ 500/T)$
3Mb	N + O + M → NO + M	3.447×10^{-45}
3Af	NO+A→N+O+A	$1.826\times10^{-13}\exp(-75\ 500/T)$
3Ab	N + O + A → NO + A	7.583×10^{-44}
4f[d]	O+NO→N+O_2	$1.389\times10^{-17}\exp(-19\ 700/T)$
4b[e]	N+O_2 →O+NO	$4.601\times10^{-15}T^{-0.546}$
5f	O+N_2 →N+NO	$1.069\times10^{-12}T^{-1.000}\exp(-37\ 500/T)$
5b	N+NO→O+N_2	$4.059\times10^{-12}T^{-1.359}$

[a]Reaction involving a molecular collision partner.
[b]Reaction involving an atomic collision partner.
[c]Reaction involving an electron as the collision partner.
[d]Forward rate for reaction mechanism.
[e]Reverse rate for reaction mechanism.

The energy of the Stardust entry is large enough to produce charged particles. The effect of the electric field is simulated simply by invoking the assumption of ambipolar diffusion and requiring the electrons to move at the average ion velocity in a given cell.[14] The vehicle surface is assumed to be fully catalytic to ions and electrons but not catalytic to atoms. The grid spacing in the direction of flow gradients is less than the local mean free path, and the computational time step is less than the local heavy particle collision time everywhere in the domain. The collision routine is subcycled within each overall simulation time step

Table 2: Reaction rate coefficients (m^3/molecule/s) used in the TCE chemistry model for reactions involving charged species.

Number	Reaction	Rate Coefficient
6f	$N+N \rightarrow N_2^+ + E^-$	$3.387\times10^{-17}\exp(-67\ 700/T)$
6b	$N_2^+ + E^- \rightarrow N+N$	$7.274\times10^{-12}T^{-0.650}$
7f	$O+O \rightarrow O_2^+ + E^-$	$1.859\times10^{-17}\exp(-81\ 200/T)$
7b	$O_2^+ + E^- \rightarrow O+O$	$1.453\times10^{-4}T^{-2.412}$
8f	$N+O \rightarrow NO^+ + E^-$	$8.766\times10^{-18}\exp(-32\ 000/T)$
8b	$NO^+ + E^- \rightarrow N+O$	$1.321\times10^{-9}T^{-1.187}$
9f	$N_2+O^+ \rightarrow O+N_2^+$	$1.511\times10^{-18}T^{0.360}\exp(-22\ 800/T)$
9b	$O+N_2^+ \rightarrow N_2+O^+$	$1.978\times10^{-18}T^{0.109}$
10f	$NO+O^+ \rightarrow O_2+N^+$	$2.324\times10^{-25}T^{1.900}\exp(-15\ 300/T)$
10b	$O_2+N^+ \rightarrow NO+O^+$	$2.443\times10^{-26}T^{2.102}$
11f	$O_2+NO^+ \rightarrow NO+O_2^+$	$3.985\times10^{-17}T^{0.410}\exp(-32\ 600/T)$
11b	$NO+O_2^+ \rightarrow O_2+NO^+$	$6.195\times10^{-16}T^{-0.050}$
12f	$N+NO^+ \rightarrow O+N_2^+$	$1.195\times10^{-16}\exp(-35\ 500/T)$
12b	$O+N_2^+ \rightarrow N+NO^+$	$1.744\times10^{-18}T^{0.302}$
13f	$O+NO^+ \rightarrow O_2+N^+$	$1.660\times10^{-18}T^{0.500}\exp(-77\ 2000/T)$
13b	$O_2+N^+ \rightarrow O+NO^+$	$2.192\times10^{-17}T^{0.114}$
14f	$N+O_2^+ \rightarrow O_2+N^+$	$1.444\times10^{-16}T^{0.140}\exp(-28\ 600/T)$
14b	$O_2+N^+ \rightarrow N+O_2^+$	$4.993\times10^{-18}T^{-0.004}$
15f	$N_2+O_2^+ \rightarrow O_2+N_2^+$	$1.644\times10^{-17}\exp(-40\ 700/T)$
15b	$O_2+N_2^+ \rightarrow N_2+O_2^+$	$4.589\times10^{-18}T^{-0.037}$
16f	$N+NO^+ \rightarrow N_2+O^+$	$5.645\times10^{-17}T^{-1.080}\exp(-12\ 800/T)$
16b	$N_2+O^+ \rightarrow N+NO^+$	$3.970\times10^{-18}T^{-0.710}$
17f	$O+NO^+ \rightarrow N+O_2^+$	$1.195\times10^{-17}T^{0.290}\exp(-48\ 600/T)$
17b	$N+O_2^+ \rightarrow O+NO^+$	$8.918\times10^{-13}T^{-0.969}$
18f	$O+O_2^+ \rightarrow O_2+O^+$	$6.641\times10^{-18}T^{-0.09}\exp(-18\ 600/T)$
18b	$O_2+O^+ \rightarrow O+O_2^+$	$4.993\times10^{-18}T^{-0.004}$
19f	$N_2+N^+ \rightarrow N+N_2^+$	$1.660\times10^{-18}T^{0.500}\exp(-12\ 100/T)$
19b	$N+N_2^+ \rightarrow N_2+N^+$	$2.343\times10^{-14}T^{-0.610}$
20	$N+E^- \rightarrow N^+ + 2E^-$	$8.434\times10^{-14}\exp(-121\ 000/T)$
21	$O+E^- \rightarrow O^+ + 2E^-$	$1.054\times10^{-14}\exp(-106\ 200/T)$

to accurately simulate collisions of electrons and heavy particles, and the particles are moved with a time step corresponding to the collision time of heavy particles. Electron-electron collisions are not simulated as these are very frequent and serve solely to thermalize the electron distribution function; it is assumed that collisions of electrons with heavy species are sufficient to do so.

III. Details of the ablation model

The following species are considered in the analysis, in addition to eleven-species air: CO, CN, C, C_2, H_2, H, C^+ and H^+. The VHS parameters used for all species are given in Table 3. Currently, the VHS parameters for the carbon and hydrogen species are simply approximations. The rates for reactions involving hydrogen and carbon containing species are obtained from the Park et al. mechanism,[15] and the reverse reaction rates are obtained using a fit to the equilibrium constants also given in that work. That chemistry model includes triatomic species, however the capability to model triatomic species is not yet implemented in the DSMC code MONACO, so those reactions are not included in these simulations. The forward and reverse reaction rates involving ablative species are given in Table 4. The temperature exponent parameter given in Ref. 15 for the electron impact ionization reactions of carbon and hydrogen, numbers 32 and 33 in Table 4, is too negative to use with the TCE chemistry model. New parameters for these reactions are found by fitting the rate given by Park, and these are given in the Table. These parameters provide good agreement with the original rates for temperatures up to about 30 000 K. Since the activation energies for these reactions are very high, it is expected that they will become important near and above the temperature limitation of the rates included here. Thus, more attention needs to be paid to either determining appropriate rates for these reactions in future work, or evaluating whether these reactions play an important role in the prediction of flowfield properties for these types of reentry flowfields. This chemistry set can eventually be updated based on a recent assessment of appropriate chemistry models for carbon-phenolic ablation[16] in these types of reentry flowfields.

Table 3: Parameters used in the VHS model.

ω	0.20		
T_{ref}	288 K		
d_{N_2}	4.07×10^{-10} m	d_{CO}	4.00×10^{-10} m
d_{O_2}	3.96×10^{-10} m	d_{CN}	4.00×10^{-10} m
d_{NO}	4.00×10^{-10} m	d_C	2.00×10^{-10} m
d_N	3.00×10^{-10} m	d_{C_2}	4.00×10^{-10} m
d_O	3.00×10^{-10} m	d_{H_2}	2.00×10^{-10} m
$d_{N_2^+}$	4.07×10^{-10} m	d_H	1.00×10^{-10} m
$d_{O_2^+}$	3.96×10^{-10} m	d_{C^+}	2.00×10^{-10} m
d_{NO}^+	4.00×10^{-10} m	d_{H^+}	1.00×10^{-10} m
d_N^+	3.00×10^{-10} m		
d_O^+	3.00×10^{-10} m		
d_e	1.00×10^{-10} m		

A particle flux of each ablating species is specified at the surface of the vehicle, and the velocity and internal energy components of each particle are calculated assuming full thermal accommodation at the surface temperature. In some simulations, both the surface temperature and blowing mass flux are varied spatially along the surface. Values of the stagnation point surface temperature and blowing rate are taken from a previous analysis of the Stardust flowfield that utilized a coupled CFD-material response technique.[3,17] The composition of the pyrolysis gas is calculated using the NASA CEA code,[18,19] assuming that it is in chemical equilibrium at the surface temperature and pressure given by the coupled CFD-material response solution. Triatomic species and species having a mass fraction of less than 0.003 are neglected in the pyrolysis gas composition. After these species are neglected, the mass fractions obtained from CEA are rescaled to sum to unity. The formation of graphite in the ablation products is not modeled, but the relative mass

Table 4: Reaction rate coefficients (m^3/molecule/s) used in the TCE chemistry model for reactions involving ablative species.

Number	Reaction	Rate Coefficient
22f	$C_2 + M \rightarrow C + C + M$	$6.14 \times 10^{-16} \exp(-69\,900/T)$
22b	$C + C + M \rightarrow C_2 + M$	2.04×10^{-46}
23f	$CN + M \rightarrow C + N + M$	$4.15 \times 10^{-16} \exp(-87\,740/T)$
23b	$C + N + M \rightarrow CN + M$	1.38×10^{-46}
24f	$H_2 + M \rightarrow H + H + M$	$3.65 \times 10^{-16} \exp(-48\,300/T)$
24b	$H + H + M \rightarrow H_2 + M$	6.07×10^{-46}
25f	$H_2 + H_2 \rightarrow H + H + H_2$	$9.13 \times 10^{-16} \exp(-48\,300/T)$
25b	$H + H + H_2 \rightarrow H_2 + H_2$	1.52×10^{-45}
26f	$CO + C \rightarrow C_2 + O$	$3.32 \times 10^{-13} T^{-1.00} \exp(-58\,000/T)$
26b	$C_2 + O \rightarrow CO + C$	$3.32 \times 10^{-14} T^{-1.00}$
27f	$O + CO \rightarrow C + O_2$	$6.48 \times 10^{-17} T^{-0.18} \exp(-69\,200/T)$
27b	$C + O_2 \rightarrow O + CO$	$1.30 \times 10^{-17} T^{-0.18}$
28f	$CO + N \rightarrow CN + O$	$1.66 \times 10^{-16} \exp(-38\,600/T)$
28b	$CN + O \rightarrow CO + N$	2.37×10^{-17}
29f	$N_2 + C \rightarrow CN + N$	$1.83 \times 10^{-16} T^{-0.11} \exp(-23\,200/T)$
29b	$CN + N \rightarrow N_2 + C$	$3.65 \times 10^{-15} T^{-0.61}$
30f	$CN + O \rightarrow NO + C$	$2.66 \times 10^{-17} T^{0.10} \exp(-14\,600/T)$
30b	$NO + C \rightarrow CN + O$	3.54×10^{-17}
31f	$CN + C \rightarrow C_2 + N$	$8.30 \times 10^{-17} \exp(-13\,000/T)$
31b	$C_2 + N \rightarrow CN + C$	$1.66 \times 10^{-12} T^{-1.00}$
32	$C + E^- \rightarrow C^+ + E^- + E^-$	$1.00 \times 10^{-11} \exp(-130\,720/T)$
33	$H + E^- \rightarrow H^+ + E^- + E^-$	$3.00 \times 10^{-12} \exp(-157\,800/T)$

fractions of the ablation products still account for its presence. The composition of the pyrolysis gas that is used in these simulations is given in Table 5. The composition of the pyrolysis products depends on the temperature and pressure at the surface of the vehicle, which varies with location along the surface. In this work, however, the composition is specified using the values given in Table 5 everywhere on the forebody surface.

Table 5: Composition of ablation products and particle flux at stagnation point.

Species	Mass fraction	Particle flux (particles/m^2/s)
CO	0.616	2.8352×10^{23}
C(s)	0.286	0
H_2	0.098	6.3147×10^{23}

In simulations where the wall temperature is variable, it is determined as follows. The stagnation point temperature is 2890 K at the 81 km trajectory point considered in this work. The mass blowing rate at this point is found to be 0.0214 kg/m^2/s. The values of surface temperature at surface locations away from the stagnation point are obtained by multiplying the stagnation temperature by the ratio of the temperature at each surface location to the stagnation temperature from a calculation that employed a radiative equilibrium wall boundary condition. The mass flux at each surface location is then determined using a relation obtained by forming a linear fit of the stagnation point ablative mass fluxes to temperatures at various trajectory points included in the analysis of Martin and Boyd.[3] The resulting profiles of surface temperature and

ablative mass flux that are used in these simulations are shown in Figure 1.

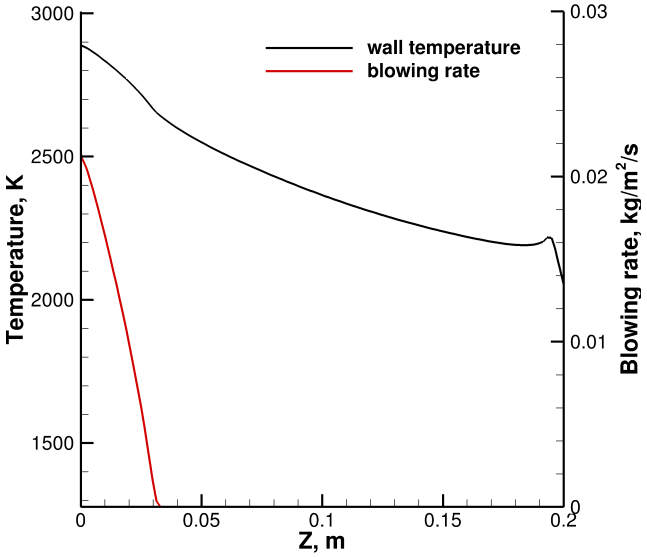

Figure 1: Wall temperature and ablative mass flux profiles imposed on the vehicle forebody surface.

As previous research has shown,[20,21] there are expected to be large differences between the CFD and DSMC flowfield predictions at this flight condition, especially in the boundary layer where gradients of the flowfield properties are large. Additionally, the boundary conditions imposed at the surface of the vehicle are fundamentally different in the present DSMC analysis as compared to the CFD-material response analysis of Martin and Boyd. Thus, this technique of determining the wall temperature and blowing rate from a coupled CFD-material response solution should eventually be replaced with more physically accurate boundary conditions by coupling the DSMC code directly to a material response code. The current work focuses on implementing the required physical models in the DSMC code to eventually permit such a coupling.

IV. Test Case: Stardust

The Stardust flight experiment is used as the baseline test case for this research. The geometry of the Stardust sample return capsule is shown in Figure 2. Axisymmetric simulation results for the flow over the entire capsule are presented in this study. The ambient conditions at the 81 km trajectory point are summarized in Table 6. The Knudsen number is computed based on the freestream mean free path and the capsule diameter. For simulations employing constant forebody surface properties, the temperature of the forebody is set to 2890 K, and the ablative mass flux is set to 0.0214 kg/m^2/s. In all simulations, the temperature of the afterbody is assumed to be 900 K, and it is assumed that the afterbody does not ablate.

Table 6: Free stream conditions for the Stardust simulation.

Altitude, km	Velocity, m/s	Mach No.	Density, kg/m^3	Temperature, K	Knudsen No.
81	12 385	42	1.27×10^{-5}	218	0.005

V. Results

In the following sections, results are presented and compared for the following cases: no ablation, ablation with constant surface temperature and mass flux of pyrolysis gas, ablation with variable surface temperature

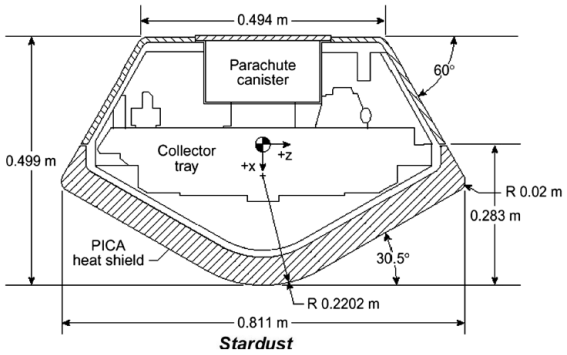

Figure 2: Geometry of the Stardust sample return capsule.

and mass flux of pyrolysis gas, ablation with variable surface properties and recombination reactions included, and ablation with ionization effects included.

The computational grid is constructed such that in the forebody region of the mesh, the cell size in the normal direction is less than a mean free path, and in the afterbody region the overall characteristic cell length is less than a mean free path. The simulation time step is less than the mean collision time everywhere in the flowfield. For the simulations that include ionization effects, the collision routine is subcycled 25 times per iteration to resolve the large electron collision rate. An example of the computational requirements are given for the case with ablation, variable surface properties, and the chemistry model that includes recombination. The axisymmetric structured grid has approximately 200 000 cells, and 1.8 million iterations are completed before sampling for 3 million iterations. The computation uses 21.2 million particles and the time step is 1.25×10^{-9} seconds. The computation took almost 8000 CPU hours on 32 nodes of an AMD Opteron cluster to complete.

A general impression of the flowfield is given in Figure 3, which shows translational temperature contours and streamlines from the simulation that included ablation, variable surface properties, recombination, and no ionization effects.

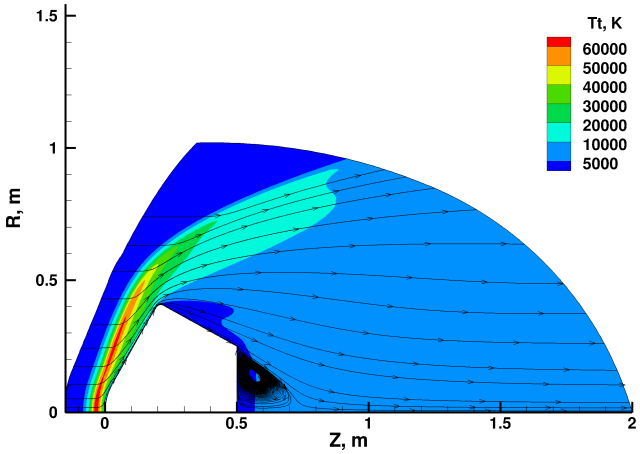

Figure 3: Translational temperature contours and streamlines in the flowfield (including ablation, variable surface properties, recombination, no ionization effects).

Figure 4 shows contours of each of the ablative species from the same simulation. The concentration of CO persists well into the wake region, while the H_2 appears to dissociate fairly close to the vehicle surface. Since the chemistry model used in this work does not include CO dissociation, the only means of breaking down the CO molecule is through exchange reactions. In future works, the effect of the omission of this reaction will be examined.

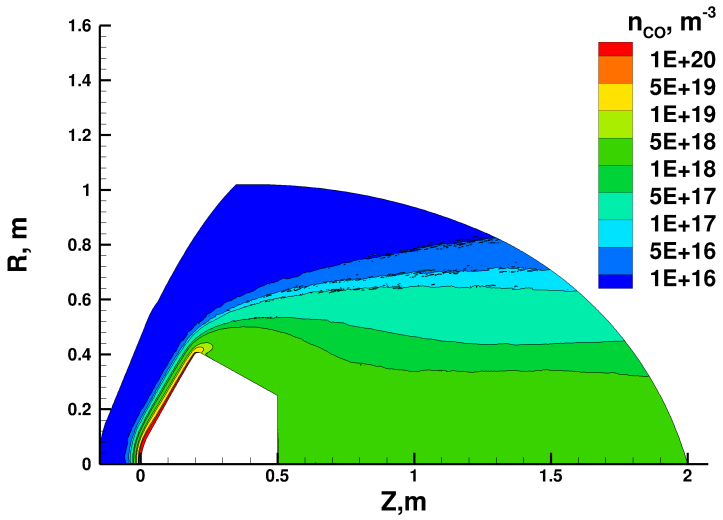

(a) Contours of CO number density.

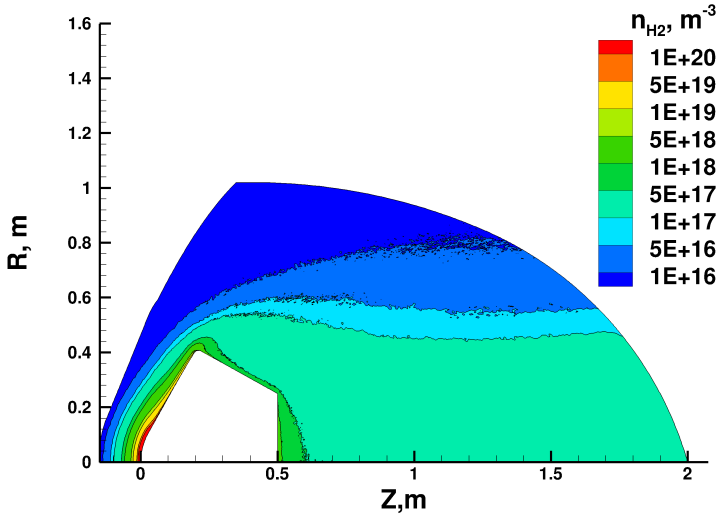

(b) Contours of H_2 number density.

Figure 4: Contours of pyrolysis gas species in the flowfield (including ablation, variable surface properties, recombination, no ionization effects).

V.A. Pyrolysis gas

The translational (Ttra), rotational (Trot) and vibrational (Tvib) temperatures along the stagnation streamline and along the wake symmetry line are shown in Figure 5 for simulations run with and without ablation effects included. There is more statistical scatter in the results obtained in the wake because the density and therefore the number of simulator particles is lower there than in the post-shock region in front of the vehicle. In general, including ablation reduces the translational and rotational temperatures in the shock layer, likely because more energy is being consumed by chemical reactions with the ablation species. Including ablation slightly increases the vibrational temperature in the shock layer, possibly due to smaller vibrational relaxation times of some of the ablation species. In the wake region, we can reliably conclude that the translational temperature when ablation is included is slightly lower than when it is not. Despite the high level of statistical scatter, it appears that the rotational and vibrational temperatures are basically unchanged from the no-ablation case.

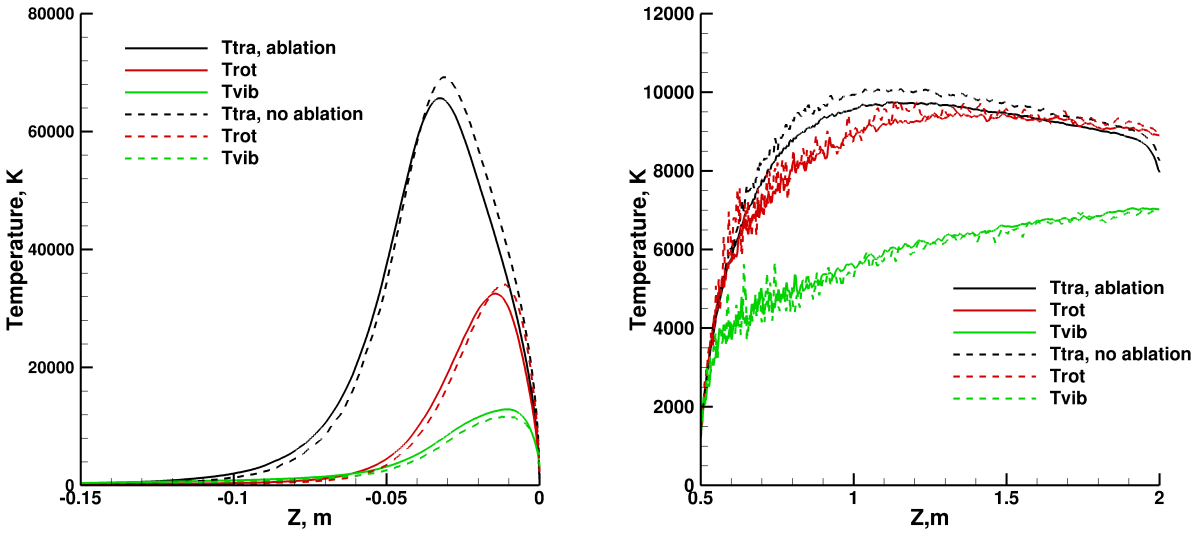

(a) Stagnation streamline.

(b) Wake symmetry line.

Figure 5: Comparison of temperatures computed with and without ablation included (variable surface properties, recombination, no ionization effects).

Figure 6 shows predicted air species concentrations along the stagnation streamline and the wake symmetry line, with and without ablation included in the simulation. In the shock layer, there is slightly less O_2 present, and slightly more N and O present when ablation is included. Along the centerline of the wake region, the concentrations of NO and N_2 increase slightly when ablation is included in the simulation. The density of O_2 is too low to appear on this Figure. Both of these effects are likely a result of the ablation species interacting with the air species in the flowfield through chemical reactions.

Lastly, Figure 7 shows the predicted heat flux along the capsule surface with and without ablation effects included in the simulation. As expected, the blowing of pyrolysis gas results in a reduction in the predicted heat flux at locations on the surface where the blowing rate is non-zero (see Figure 1). This is because the boundary layer is thickened by the incoming momentum resulting in a reduction in the temperature gradient at the surface. The presence of species containing carbon and hydrogen also changes the gas conductivities, and this also affects the predicted heat flux. Since no chemical reactions or catalytic reactions on the surface are modeled in these cases, the heat flux component due to species diffusion at the surface is not affected. The predicted heat flux along the afterbody is much smaller than that along the forebody and is relatively unchanged by the consideration of ablation in the simulation.

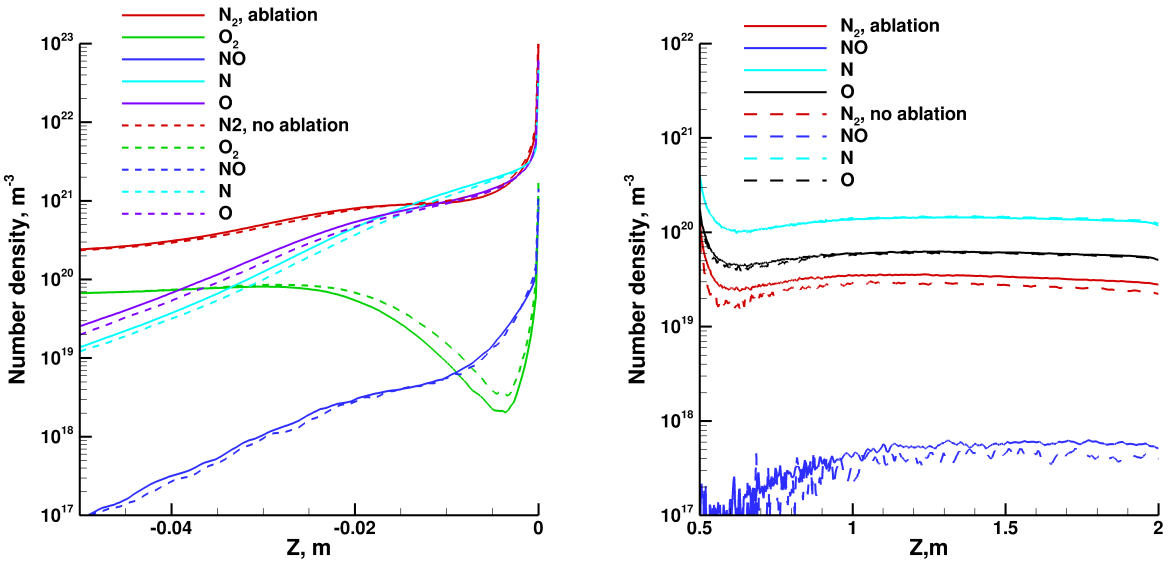

(a) Stagnation streamline.

(b) Wake symmetry line.

Figure 6: Comparison of air species densities computed with and without ablation included (variable surface properties, recombination, no ionization effects).

V.B. Variable surface properties

To test the effect of modeling the variation of surface temperature and ablative mass flux along the surface, a simulation is run in which the forebody surface properties are held constant at a wall temperature of 2890 K and a pyrolysis mass flux of 0.0214 kg/m^2/s. As expected, neglecting any variation of these properties along the surface results in very different flowfield predictions. Figure 8 shows the predicted temperatures along the stagnation streamline for the cases with constant and variable surface properties. When the surface properties are held constant, the shock stand-off distance (as indicated by the temperature profiles) increases relative to the case that employs variable surface properties. This changes the shape and magnitude of the air species density profiles, which are shown in Figure 9(a). In general, there is more dissociated nitrogen and oxygen in the flowfield when the surface properties are held constant at the stagnation temperature.

Figure 9(b) shows the density of ablation species in the flowfield; the densities of all species except H_2 are larger throughout the flowfield in the constant surface property case. This is simply because the imposed ablative mass flux is linearly proportional to temperature in our simulations, so a higher surface temperature results in a larger mass flux. Temperature and species density profiles are not shown along the wake symmetry line, since the general trends are the same as those along the stagnation streamline.

V.C. Recombination reactions

The recombination reactions are originally omitted from the analysis to reduce the complexity. A simulation with pyrolysis gas and variable surface properties is run including those reactions, which are labelled 1b, 2b, 3b, 22b, 23b, 24b and 25b in Tables 1 and 4. The species concentrations along the stagnation streamline and surface heat flux predictions are essentially unchanged between the two simulations. Figure 10 shows a comparison of the predicted air species and ablation species along the wake symmetry line. Some species with very low concentrations are omitted. From these results we can see that if one is concerned with species concentrations in the wake region, then the recombination reactions should be included in the simulation. For example, the predicted density of the CO molecule in the wake is approximately ten times higher in the simulation that includes recombination reactions.

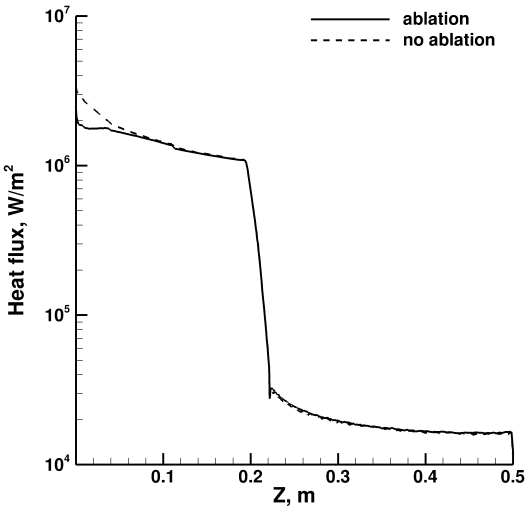

Figure 7: Heat flux along capsule surface with and without ablation included (variable surface properties, recombination, no ionization effects).

V.D. Ionization effects

As stated earlier, due to the high velocity of the Stardust capsule during its reentry into the atmosphere, collisions between particles are energetic enough to cause ionization reactions. Thus, the chemistry mechanism is extended to include the following charged species: N_2^+, O_2^+, NO^+, N^+, O^+, C^+ and H^+ and the associated reactions. As expected, the results indicate that the vibrational and electron translational temperatures are in equilibrium throughout the flowfield. Other than that, the trends discussed in Section V.A regarding the behaviour of flowfield temperatures and surface heat flux when ablation is considered are repeated here, so those results are not shown.

Figure 11 shows the concentrations of ions and electrons both along the stagnation streamline and along the wake symmetry line. In the boundary layer along the stagnation streamline, the concentrations of ions and electrons are larger in the simulation that does not include ablation. This is likely because energy that may be used to ionize particles is instead used in reactions with ablative species when ablation is included. The concentrations of H^+ and C^+ are also shown; the concentration of C^+ is very low relative to the other species; however, since the ionization rate for this reaction is estimated using an expression that becomes inaccurate at high temperatures, the validity of this result should be explored further. Along the wake symmetry line, the predicted ion and electron densities with and without ablation are generally very similar. The densities of O_2^+ and C^+ are too low to be shown in this figure. The large amount of statistical scatter in the results obtained near the vehicle surface is a result of a lack of sufficient particles in that region to accurately model the trace species (ie: NO, CO, CN, N_2^+, e, NO^+, H^+). A solution for this issue needs to be addressed in future work.

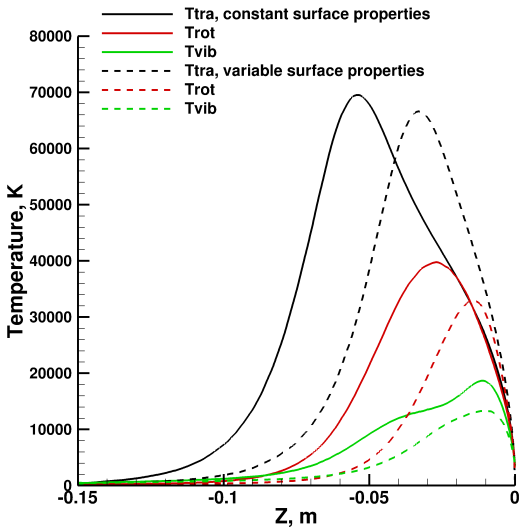

Figure 8: Temperatures along the stagnation streamline computed with and without variable surface properties (including ablation, recombination, no ionization effects).

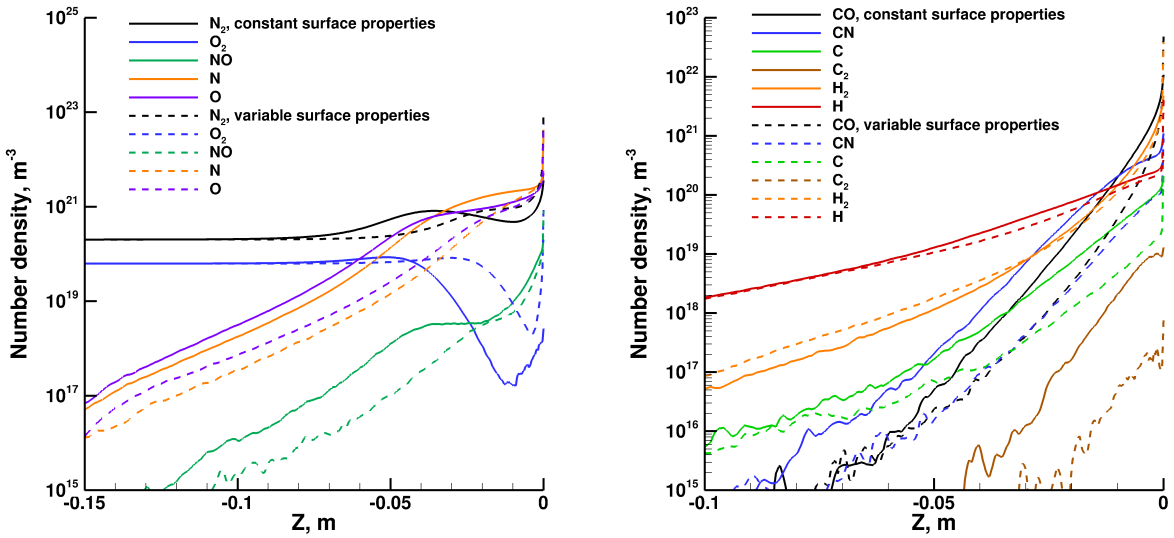

(a) Air species.

(b) Ablation species.

Figure 9: Comparison of species densities along the stagnation streamline computed with and without variable surface properties (including ablation, recombination, no ionization effects).

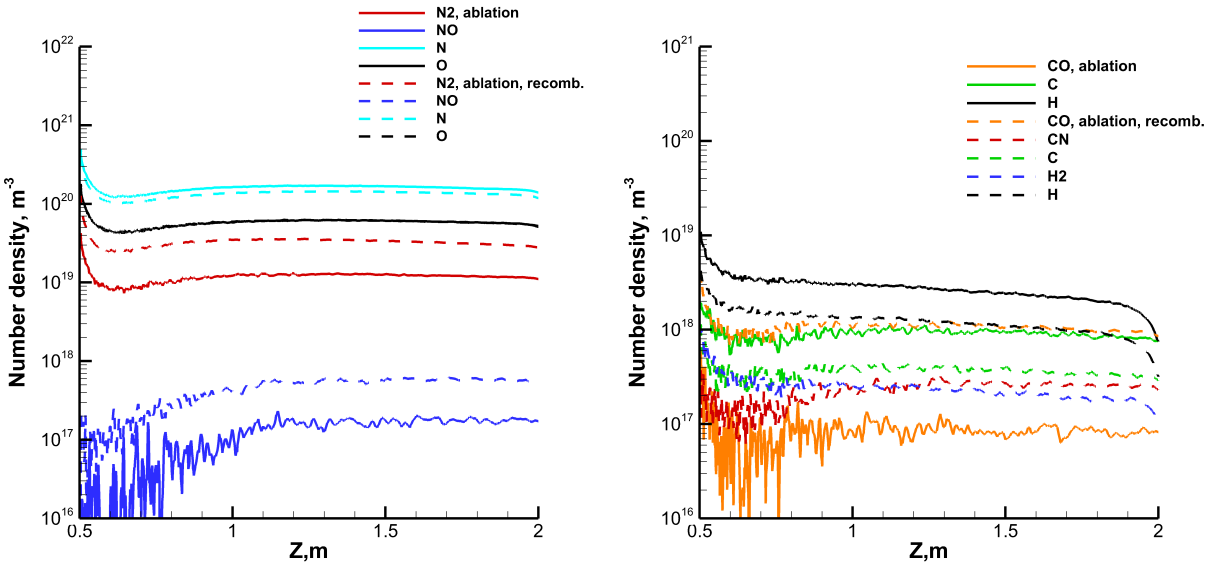

(a) Air species.

(b) Ablation species.

Figure 10: Comparison of species densities along the wake symmetry line computed with and without recombination reactions included (including ablation, variable surface properties, no ionization effects).

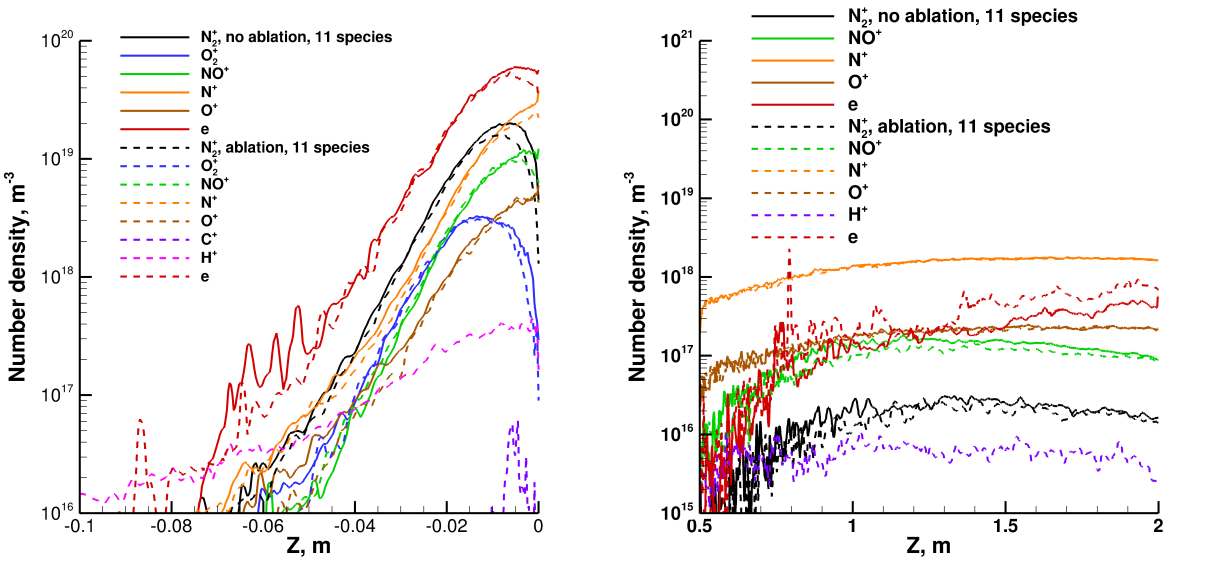

(a) Stagnation streamline.

(b) Wake symmetry line.

Figure 11: Comparison of ion and electron densities along the stagnation streamline and wake symmetry line computed with ionization effects included (including ablation, variable surface properties, no recombination).

VI. Conclusions

This paper details an on-going effort to include the effects of a charring, ablating capsule surface on predictions of macroscopic flowfield properties in hypersonic entry under rarefied conditions. The expected reduction of surface heat flux with the addition of the ejection of pyrolysis gas into the flow has been demonstrated. We have demonstrated the importance of including recombination reactions in these types of simulations, and as expected, confirmed that modeling the variable nature of the surface properties has a non-negligible effect on the flowfield predictions.

It is clear that more work needs to go into developing good physical models for species interactions and chemical reactions required to model ablating carbon phenolic materials using the DSMC method. Perhaps one of the most important conclusions of this paper is that variable species weighting of some sort is required to reduce the statistical scatter in the results and accurately compute these types of flowfields, which by their nature, produce species in very disparate concentrations. Additionally, the experience gained during these DSMC simulations of the flowfield around the *entire* re-entry capsule, including a large number of species and chemical reactions, has emphasized the need for a more efficient way of treating the electron species during the computation.

VII. Future Work

There are many areas in which the current simulation capability can be improved. They include:

- improved VHS model parameters for species containing carbon and hydrogen,
- improved reaction rates for carbon and hydrogen electron impact ionization reactions for use with the DSMC method,
- inclusion of triatomic species in the chemistry model,
- investigation of alternate chemistry mechanisms for modeling ablation products,
- addition of a species weighting scheme to reduce the computational cost of the simulation and increase the accuracy of the results,
- an improved method of electron simulation to reduce computational time.

In terms of physical models for ablation processes, the next long-term steps are to develop and couple a finite-rate surface chemistry model to the DSMC code, and to couple the DSMC code to a material response module.

Acknowledgments

This work is partially funded by NASA grant NCC3-989. The authors wish to thank Dr. Ioana Cozmuta of NASA Ames Research Center for making the DPLR-FIAT-MAT solutions for the Stardust trajectory available.

References

[1]M. Stackpoole, S. Sepka, I. C. and Kontinos, D., "Post-flight Evaluation of Stardust Sample Return Capsule Forebody Heatshield Material," *AIAA Paper 2008-1202*, presented at the 46th AIAA Aerospace Sciences Meeting and Exhibit, Reno, NV, Jan. 2008.

[2]Olynick, D., Chen, Y.-L., and Tauber, M. E., "Aerothermodynamics of the Stardust Return Capsule," *Journal of Spacecraft and Rockets*, Vol. 36, No. 3, 1999, pp. 442–462.

[3]Martin, A. and Boyd, I. D., "CFD Implementation of a Novel Carbon-Phenolic-in-Air Chemistry Model for Atmospheric Re-entry," *AIAA-2011-143*, presented at the 49th AIAA Aerospace Sciences Meeting and Exhibit, Orlando, FL, Jan. 2011.

[4]Zhong, J., Ozawa, T., and Levin, D. A., "Modeling of Stardust Reentry Ablation Flows in the Near-Continuum Flight Regime," *AIAA Journal*, Vol. 46, No. 10, 2008, pp. 2568–2581.

[5]Dietrich, S. and Boyd, I. D., "Scalar and Parallel Optimized Implementation of the Direct Simulation Monte Carlo Method," *Journal of Computational Physics*, Vol. 126, No. 0401, 1996, pp. 328–342.

[6]Bird, G. A., "Monte Carlo Simulation in an Engineering Context," *Rarefied Gas Dynamics*, edited by S. S. Fisher, Vol. 74 of *Progress in Astronautics and Aeronautics*, AIAA, New York, 1981, pp. 239–255.

[7]Boyd, I. D., "Rotational-translational Energy Transfer in Rarefied Nonequilibrium Flows," *Physics of Fluids*, Vol. 2, No. 3, 1989, pp. 447–452.

[8]Boyd, I. D., "Analysis of Vibrational-translational Energy Transfer Using the Direct Simulation Monte Carlo Method," *Physics of Fluids*, Vol. 3, No. 7, 1991, pp. 1785–1791.

[9]Park, C., "Review of Chemical-Kinetic Problems of Future NASA Missions, I: Earth Entries," *Journal of Thermophysics and Heat Transfer*, Vol. 7, No. 3, 1993, pp. 385–398.

[10]Boyd, I. D., "Modeling of Associative Ionization Reactions in Hypersonic Rarefied Flows," *Physics of Fluids*, Vol. 19, 2007, pp. 096102.

[11]Wilson, J., "Ionization Rate of Air Behind High-speed Shock Waves," *Physics of Fluids*, Vol. 9, No. 10, 1966, pp. 1913–1921.

[12]Bose, D. and Candler, G., "Thermal Rate Constants of the N_2+O $\rightarrow$ NO + N Reaction Using Ab Initio ^{3}A" and ^{3}A' Potential Energy Surfaces," *Journal of Chemical Physics*, Vol. 104, No. 8, 1996, pp. 2825–2833.

[13]Haas, B. L. and Boyd, I. D., "Models for Direct Monte Carlo Simulation of Coupled Vibration-Dissociation," *Physics of Fluids*, Vol. 5, No. 2, 1993, pp. 478–489.

[14]Boyd, I. D., "Monte Carlo Simulation of Nonequilibrium Flow in a Low-power Hydrogen Arcjet," *Physics of Fluids*, Vol. 9, No. 10, 1997, pp. 4575–4584.

[15]Park, C., Jaffe, R. L., and Partridge, H., "Chemical-Kinetic Parameters of Hyperbolic Earth Entry," *Journal of Thermophysics and Heat Transfer*, Vol. 15, No. 1, 2001, pp. 76–90.

[16]Martin, A. and Boyd, I. D., "Assessment of Carbon-Phenolic-In-Air Chemistry Models for Atmospheric Re-entry," *AIAA-2010-4656*, presented at the 10th AIAA/ASME Joint Thermophysics and Heat Transfer Conference, Chicago, IL, June 2010.

[17]Martin, A., Boyd, I. D., Cozmuta, I., and Wright, M. J., "Chemistry Model for Ablating Carbon-Phenolic Material During Atmospheric Re-entry," *AIAA-2010-1175*, presented at the 48th AIAA Aerospace Sciences Meeting and Exhibit, Orlando, FL, Jan. 2010.

[18]Gordon, S. and McBride, B. J., "Computer Program for Calculation of Complex Chemical Equilibrium Compositions and Applications I: Analysis," Tech. Rep. NASA Reference Publication 1311, 1994.

[19]Gordon, S. and McBride, B. J., "Computer Program for Calculation of Complex Chemical Equilibrium Compositions and Applications II: Users Manual and Program Description," Tech. Rep. NASA Reference Publication 1311, 1996.

[20]Boyd, I. D., Trumble, K., and Wright, M. J., "Modeling of Stardust Entry at High Altitude, Part 1: Flowfield Analysis," *Journal of Spacecraft and Rockets*, Vol. 47, No. 5, 2010, pp. 708–717.

[21]Boyd, I. D. and Jenniskens, P., "Modeling of Stardust Entry at High Altitude, Part 2: Radiation Analysis," *Journal of Spacecraft and Rockets*, Vol. 47, No. 6, 2010, pp. 901–909.